Quantifying vanadium-vacancy clusters in V2O3 towards ultra-long cycling aqueous zinc-ion battery

Zhu Kefu
University of Science and Technology of China
Shiqiang Wei
National Synchrotron Radiation Laboratory, CAS Center for Excellence in Nanoscience, University of Science and Technology of China, Hefei, Anhui
Hongwei Shou
University of Science and Technology of China
Fei-Ran Shen
Institute of Physics, Chinese Academy of Sciences
Shuangming Chen
University of Science and Technology of China
Zhang Pengjun
University of Science and Technology of China
Wang Changda
University of Science and Technology of China
Cao Yuyang
University of Science and Technology of China
Guo Xin
University of Science and Technology of China
Mi Luo
University of Science and Technology of China
Hongjun Zhang
University of Science and Technology of China
Bang-Jiao Ye
University of Science and Technology of China
Xiaojun Wu
University of Science and Technology of China https://orcid.org/0000-0003-3606-1211
LunHua He
Institute of Physics
Li Song (song2012@ustc.edu.cn)
University of Science and Technology of China https://orcid.org/0000-0003-0585-8519

Article

Keywords: Defect Engineering, Rietveld Analysis, Neutron Powder Diffraction, X-ray Powder Diffraction, Positron Annihilation Spectroscopy, Electrostatic Interaction, Storage Performance

Posted Date: May 3rd, 2021

DOI: https://doi.org/10.21203/rs.3.rs-438552/v1

Version of Record: A version of this preprint was published at Nature Communications on November 25th, 2021. See the published version at https://doi.org/10.1038/s41467-021-27203-w.

Quantifying vanadium-vacancy clusters in V_2O_3 towards ultra-long cycling aqueous zinc-ion battery

Kefu Zhu[1,7], Shiqiang Wei[1,7], Hongwei Shou[1,7], Feiran Shen[4,5,7], Shuangming Chen[1,*], Pengjun Zhang[1], Changda Wang[1], Yuyang Cao[1], Xin Guo[1], Mi Luo[2], Hongjun Zhang[2], Bangjiao Ye[2], Xiaojun Wu[3], Lunhua He[4,5,6,*], Li Song[1,*]

[1] National Synchrotron Radiation Laboratory, CAS Center for Excellence in Nanoscience, University of Science and Technology of China, Hefei, 230029, China
[2] State Key Laboratory of Particle Detection and Electronics & Hefei National Laboratory for Physical Sciences at the Microscale, University of Science and Technology of China, Hefei, 230026, China
[3] School of Chemistry and Material Sciences, University of Science and Technology of China, Hefei, 230026, China
[4] Beijing National Laboratory for Condensed Matter Physics, Institute of Physics, Chinese Academy of Sciences, Beijing, 100190, China
[5] Spallation Neutron Source Science Center, Dongguan, 523803, China
[6] Songshan Lake Materials Laboratory, Dongguan, 523808, China
[7] These authors contribute equally.
* Correspondence: Shuangming Chen (csmp@ustc.edu.cn),
Lunhua He (lhhe@iphy.ac.cn),
Li Song (song2012@ustc.edu.cn)

Abstract

Defect engineering has been attracted widespread attention for promoting the stability of the electrodes. However, accurately quantifying and defining the effect of defects is extremely difficult. Here, the Rietveld analysis with combined neutron powder diffraction (NPD) and X-ray powder diffraction (XRD) patterns reveal vanadium defect (V_d) clusters in the V_2O_3 lattice up to 5.7% in aqueous zinc-ion batteries (ZIBs), further confirmed by positron annihilation spectroscopy (PAS) and synchrotron-based X-ray analysis. Benefitting from the V_d clusters, the V_2O_3 cathode achieves excellent cycle life with 81% capacity retention at 5.0 A g^{-1} after 30,000 cycles that is the most superb stable cathode for aqueous ZIBs at this current density. Besides, the density functional

theory (DFT) calculations strongly indicate that the V_d clusters not only provide permanent sites for Zn^{2+} anchormen to enhance the integrity of V_2O_3 after the first discharging process, but also make Zn^{2+} de/intercalation in complex oxide, contributing collectively and effectively reducing the strong electrostatic interaction between host multivalent ions, resulting in the remarkable storage performance of Zn^{2+}. This work highlights accurately quantifying and identifying the significant effect of defects for designing cathodes with ultra-long cycle life in future intelligent devices.

Introduction

With the increase of energy crisis and environmental pollution problems, it is essential to develop green and clean energy storage devices. As a bellwether in the field of energy storage, lithium-ion batteries (LIBs) are a key technique in advanced power technologies[1,2]. However, emerging worries are their limited lithium resources and security issues towards future large-scale applications[3-6]. Encouragingly, rechargeable aqueous ZIBs have emerged as the most promising complements to LIBs regarding high specific capacity (819 mA h g^{-1}), low cost, abundant resources, and environment friendly[7-9]. It has been demonstrated that aqueous ZIBs have been applied in miniaturized electronic devices, such as epidermis, implantable and wearable sensors[10-12], indicating that aqueous ZIBs have great commercial potential. But great upgrading is needed to put it into a widespread application. The most compelling issue is to seek long-cycling cathodes for aqueous ZIBs due to serious consequences of stability penalty caused by the aqueous system and bigger ionic radius of Zn^{2+}. Defect engineering has been regarded as an availability approach for promoting the stability of

electrodes, where the strong electrostatic interaction between the host and multivalent ions with a greater charge can be efficiently reduced, accelerate the reaction kinetics and facilitate the reversible storage of Zn ions[13-16]. Particularly, the research of defects in oxide electrodes most used for ZIBs is required due to the complex composition and the dynamic process during the working process. Accurately quantification of material defects is essential to determine the metal vacancies and oxygen vacancies at the same time. However, it is extremely hard to simultaneously determine the concentration of two vacancies. For example, light oxygen is difficult to be detected by XRD owing to its small atomic radius, compared with most metal elements. Consequently, the joint application of multiple spectroscopy is essential to accurately quantify defects.

In this work, we have quantified for the first time in aqueous ZIBs that V_2O_3 (V_d-V_2O_3) electrode contains 5.7% V_d clusters by Rietveld analysis with combined XRD and NPD patterns. It is the V_2O_3 cathode containing V_d clusters that delivers ultra-long cycling stability (81% retention after 30,000 cycles at a current density of 5 A g^{-1}), which is the longest cycling stability for the aqueous ZIBs cathode to date. Accurately quantifying and identifying the effect of defects provides a new path for the design of cathodes with long stability for energy storage devices.

Structure and morphology characterization of V_d-V_2O_3

The V_d-V_2O_3 cathode was designed by a hydrothermal method and an ensuing annealing process (see Supplementary Information for details). Scanning electron microscopy (SEM, **Supplementary Fig. 1**) and Transmission electron microscope (TEM, **Supplementary Fig. 2a**) images show that the V_d-V_2O_3 is a uniform flower-like

hierarchical structure assembled by thin nanosheets with a size of around 100-200 nm. In the high-resolution TEM (**Supplementary Fig. 2b**) image of the flower-liked V_d-V_2O_3, a lattice fringe with a layer spacing of d = 0.27 nm was found, corresponding to the (104) lattice plane. The surface area and pore size were detected by BET (Brunauer-Emmett-Teller) characterization, the V_d-V_2O_3 has a high surface area of 60.34 m^2 g^{-1} and a large pore size of about 22 nm (**Supplementary Fig. 3**). A large surface area can provide sufficient contact between the electrode and electrolyte and shorten the Zn^{2+} diffusion path time. The mesoporous structure is advantageous to the insertion and extraction of Zn^{2+}, which can effectively improve the cycle life of the battery.

For detailed structure information, X-ray absorption fine structure (XAFS) was performed to investigate the local fine structure of V_d-V_2O_3. As illustrated in the XANES spectra of V K-edge (**Fig. 1a** inset), the absorption edge of the V_d-V_2O_3 is found to shift toward higher energy (Site B) compared with commercial V_2O_3 (c-V_2O_3), stating clearly that V_d-V_2O_3 possesses a higher average valence state. The high-resolution XPS of V 2p further shows that despite the valence states of V in V_d-V_2O_3 and c-V_2O_3 are +3 and +4 coexistence (**Supplementary Fig. 4**), the content of V^{4+} is larger (**Supplementary Table 1**). The identical result can be gotten from electron paramagnetic resonance (EPR) spectroscopy, where the EPR signal of tetravalent vanadium has a stronger response strength[17,18] (**Supplementary Fig. 5**). It has been reported that the surface of V_2O_3 is vulnerable to be oxidized to V^{4+}, which explains the existence of V^{4+} in c-V_2O_3[19,20]. But the situation in V_d-V_2O_3 is different, the surface of V_d-V_2O_3 is proved to be uniformly coated with carbon (**Supplementary Figs. 6 and 7**).

Thermogravimetric analysis (TGA) shows that the carbon content is 19.36% (**Supplementary Fig. 8**). Surface coated with the carbon of V_d-V_2O_3 is believed to be not easily oxidized, so the higher content of V^{4+} in V_d-V_2O_3 may attribute to the existence of vanadium vacancies, which leads to a valence increase of V. The pre-edge peak in the XANES of V K-edge corresponds to the electronic transition from 1s to $3d^{21}$, which can promulgate the local structure symmetry. As shown in **Fig. 1a** inset (Site A), the increase of pre-edge peak intensity attributes to the decrease of local symmetry of V_d-V_2O_3. That is suggested that the structure of V_d-V_2O_3 is distorted around V atoms, owing to the absence of surrounding atoms. To further obtain the accurate coordination numbers (CN), the corresponding Fourier transformed EXAFS is fitted that is shown in **Supplementary Fig. 9** and the detailed fitting results can be found in **Supplementary Table 2**. The results demonstrate that the CN of the V-V in V_d-V_2O_3 is significantly lower than that in c-V_2O_3 (2.2 vs. 4), which exhibits that there are vanadium vacancies in V_d-V_2O_3.

In order to further corroborate the defect situation in V_d-V_2O_3, we used PAS to explore the defect type and concentration of the material[22]. **Table 1** shows the positron annihilation lifetime data of V_d-V_2O_3 and c-V_2O_3. There are three life components (τ_1, τ_2, and τ_3), among which τ_1, τ_2, and τ_3 correspond to defect-free bulk region and the tiny vacancies, vacancy clusters, and interfaces (free space between nanograins) in the material, respectively[23,24]. Due to the microscopic sizes of both V_d-V_2O_3 and c-V_2O_3 are above 500 nm (**Supplementary Figs. 1 and 10**), there exist considerable amount of vacancy clusters in both samples. It is noteworthy that the intensity I_2 of τ_2 for V_d-

V_2O_3 is 78.01%, which is much higher than that of c-V_2O_3, indicating that the concentration of vacancy clusters in V_d-V_2O_3 is much higher than that in c-V_2O_3. The PALS results provide reliable and valuable proof of the coexistence of vanadium vacancies with a relatively high concentration in V_d-V_2O_3, and the phenomenon of defect aggregation may occur, also revealed by DFT.

For accurately determine the type and concentration of defects, we combined NPD and XRD techniques. In the V_d-V_2O_3 cathode, the neutron scattering amplitude of V element is just -0.3438cm^{-12} and the atomic radius of light oxygen element is about 0.66Å. As a result, the scattering factor of the vanadium element in the V_d-V_2O_3 cathode is too small to be detected by NPD, while the light oxygen element is hard to be probed by XRD. Therefore, Rietveld analysis with combined XRD and NPD patterns was conducted to reveal the crystal structure information (**Fig. 1c**). The refinement results (**Supplementary Table 3**) and show that, the V_d-V_2O_3 has a typical corundum-type hexagonal structure (Space group: R - 3 c) with lattice parameters to be a=b=4.9473(1) Å, c=13.9990(5) Å. The V and O atoms occupy the 12c (0, 0, 0.15437(6)) and 18e (0.3145(3), 0, 0.25) crystallographic positions, respectively. Moreover, the occupancy rate of vanadium atoms at 12c sites is about 94.3(1) %, while no oxygen vacancy was detected at 18e sites (**Fig. 1b**). In general, we have demonstrated the presence of coordinately unsaturated atoms of V in V_d-V_2O_3 and the vacancy occupancy rate of vanadium is 5.7%, and the vanadium vacancies exist in the form of vacancy clusters.

Electrochemistry

To investigate the Zn^{2+} storage performance of the V_d-V_2O_3 cathode, the 2032 type

coin-cells were assembled using a zinc foil anode, a 3 M $Zn(CF_3SO_3)_2$ electrolyte (**Supplementary Figs. 11 and 12**), and a filter paper separator. As shown in **Supplementary Fig. 13**, the cyclic voltammetry (CV) curves of the V_d-V_2O_3 electrode are carried out at a scan rate of 0.1 mV s^{-1} within a voltage window of 0.1-1.3 V (vs Zn/Zn^{2+}). Two pairs of redox peaks located at 1.09/0.78 V and 0.93/0.53 V are observed, which attributes to a two-step (de)intercalation process of Zn^{2+}. The rate performance for V_d-V_2O_3 at current densities from 0.1 to 4.0 A g^{-1} is presented in **Fig. 2a** and **Supplementary Fig. 14**. The reversible capacities of the V_d-V_2O_3 electrode are 196, 187, 165, 147, 138, 125, 117 and 113 mA h g^{-1} at the current densities of 0.1, 0.3, 0.5, 0.8, 1.0, 2.0, 3.0, and 4.0 A g^{-1}, respectively. When current density returns to 0.5 A g^{-1}, a specific capacity of 163 mA h g^{-1} is restored which ulteriorly illustrates the high electrochemical reversibility of the V_d-V_2O_3 electrode. The capacity retention reaches 70.4% when the current densities increase from 0.1 to 1.0 A g^{-1}, exhibiting excellent rate capability. It is ecstatic that the V_d-V_2O_3 electrode delivers ultra-long cycling stability with a capacity retention rate of 98% after 10,000 cycles, 90% after 20,000 cycles, and 81% after 30,000 cycles at a current density of 5 A g^{-1} **(Fig. 2b)**. To the best of our knowledge, the cycling stability of 30,000 cycles is the longest cycle lifetime for reported ZIBs at this current density. As shown in **Fig. 2c**, the life span of V_d-V_2O_3 is superior to most of the other aqueous ZIBs (**Supplementary Table 4**) recently reported in pieces of literature[25-30]. These results certainly highlight the great potentials of V_d-V_2O_3 cathode-based Zn batteries in the field of smart energy storage devices. The longevity of this V_d-V_2O_3 cathode comes ultimately from abundant vacancy clusters

that attenuate the strong electrostatic interaction between Zn^{2+} and the V_d-V_2O_3 host. As shown in **Supplementary Fig. 15**, the c-V_2O_3 cathode, without vacancies, demonstrates inferior both rate and stability electrochemical performance for aqueous ZIBs, which strongly confirms the positive effects of vacancies in V_d-V_2O_3 cathode.

To further understand the greatly enhanced Zn^{2+} storage performance, the electrochemical kinetics of the V_d-V_2O_3 electrode was investigated. As shown in **Fig. 2d**, CV measurements are carried out at different scan rates. With the increase of scan rates from 0.1 to 1.0 mV s^{-1}, the CV curves show a similar shape and the reduction and oxidation peaks are well preserved. Regularly, the peak currents (*i*) and their corresponding sweep rates (*v*) obey a power-law relationship that is described by

$$i = av^b, \quad (1)$$

Where *i* represents the peak current (A), *v* represents the scan rate (V s^{-1}) and *a*, *b* are constants. The b values are useful as the base for analyzing electrochemical processes, where the b value is equal to 0.5 indicates that the electrochemical process is governed by ionic diffusion, and a capacitive storage process is indicated when *b* value is 1.0. From the equation of log (*i*) = blog (*v*) + log (*a*) derived from equation (1), the calculated *b*-values for both cathode and anode peaks from CV curves are 0.94, 0.75, 0.79, and 0.88, respectively (**Fig. 2e**). It is suggested that the Zn^{2+} storage behavior of V_d-V_2O_3 is controlled collectively by ionic diffusion and capacitive, which leads to fast Zn^{2+} diffusion kinetics enabling the high-rate performance. In order to further quantify the contribution of diffusion-controlled and capacitive-controlled at a specific scan rate, equation (1) is divided into two halves to form formula (2):

$$i(V) = k_1 v + k_2 v^{1/2} \quad (2)$$

According to the above equation, the current (i) at a specific potential (V) can be divided into a capacitance limiting effect (k_1v) and a diffusion control effect ($k_2v^{1/2}$). As shown in **Supplementary Fig. 16**, the capacitance contribution (corresponding to the purple region) is 82.5% of the overall contribution at scan rate 0.8 mV s^{-1}. With the increases of scan rates from 0.1 to 1 mV s^{-1}, the capacitance contribution rates increase from 66.3% to 86.4% (**Fig. 2f**). This suggests a substantially greater proportion of capacitive-dominated process, which directly contributes to excellent rate performance due to the fast kinetics of Zn^{2+}. Galvanostatic intermittent titration technique (GITT) is performed to analyze the diffusion coefficient of Zn^{2+} in the V_d-V_2O_3 electrode (**Supplementary Fig. 17**). The result shows that the diffusion coefficient of Zn^{2+} in the V_d-V_2O_3 electrode is between 10^{-7}-10^{-8} cm^2 s^{-1}, which stays ahead of the other existing electrodes[6,31,32].

Zinc-ion storage mechanism of V_d-V_2O_3

DFT calculations were conducted to explore the veritable function of V_d-V_2O_3 for Zn^{2+} storage. To investigate the distribution of vanadium vacancies, based on the XRD and NPD Rietveld analysis results, diverse vanadium vacancy models at the concentration of 6.25%, in good agreement with experiments were constructed as shown in **Supplementary Fig. 18**. A lower formation enthalpy represents a more stable phase. Structure 1 possesses the smallest formation enthalpy, illustrating the short aggregation of V_d clusters which is consistent with **Table 1**. Then, the p-V_2O_3 and V_d-V_2O_3 were implemented to disclose the insertion of Zn^{2+}. The frustrated insertion of Zn^{2+} into p-V_2O_3 was observed due to the enormously positive Gibbs free energy (2.69 eV)[33],

illustrating no capacity or an extremely tiny capacity (**Fig. 3a**), consistent with the badly Zn^{2+} storage performance of c-V_2O_3 (**Supplementary Fig. 15**). What's more, the direct insertion of Zn^{2+} into p-V_2O_3 may cause the destruction of the structure, leading to bad stability. However, for V_d-V_2O_3, vanadium vacancies will accept the insertion of Zn^{2+} and provide high capacity than c-V_2O_3. Intriguingly, the distinguishing Gibbs free energies demonstrate the process of insertion of Zn^{2+} into V_d-V_2O_3 is different. Firstly, the vanadium defect is occupied with Zn^{2+} and a large number of heat was released (-1.34 eV) due to the strong electrostatic, improving the integrities and stabilities of V_d-V_2O_3. Nevertheless, due to this strong electrostatic interaction, the extraction of this kind Zn^{2+} is unbearable, demonstrating the self-anchoring action of Zn^{2+} in the lattice. Secondly, the feasible and sustainable insertion of Zn^{2+} into V_d-V_2O_3 is observed, affording the capacity and voltage **(Fig. 3a)**. This phenomenon unravels the residual of Zn in V_d-V_2O_3. Consequently, the dual-effect of vanadium vacancies in V_d-V_2O_3 is specified in **Fig. 3b**. When Zn^{2+} initially entries into the V_d-V_2O_3 electrode that has many vanadium vacancies, part of Zn^{2+} will be riveted on vanadium vacancies and caged inside during the whole time. In other words, the eventual structure is a Zn doped V_d-V_2O_3 after the first discharging self-optimized process, in which the Zn^{2+} will reversibly insert or leave in the subsequent cycles.

Based on the above analysis, a series of characterizations were conducted to demonstrate the Zn^{2+} storage mechanism of the V_d-V_2O_3 cathode and effect of vanadium vacancies. It can be seen from **Figs. 4a** and **4b** that the characteristic (104) and (110) peaks move to a lower 2θ degree during the discharging process and return

to the original position in the subsequent charge process. These reversible movements originate from the expansion and contraction of the lattice of V_d-V_2O_3 with the de/intercalation of Zn^{2+}. Besides, no other diffraction peaks were detected, indicating no phase transformations in the V_d-V_2O_3 electrodes during the charge/discharge process. The stability of V_d-V_2O_3 was further incarnated in the unchanged XRD curves after 500 cycles (**Supplementary Fig. 19**). It is noteworthy that the morphology of the V_d-V_2O_3 electrodes have transformed into particles with a diameter of about 25 nm after the first cycle and remained unchanged in the subsequent cycles, which adapts to the reversible insertion/extraction of Zn^{2+} better. (**Supplementary Figs. 20-22**).

X-ray photoelectron spectroscopy (XPS) and soft X-ray absorption spectrum (sXAS) were performed to give insight into the chemical states of the V_d-V_2O_3 electrodes at different states. The reversible insertion and extraction of Zn^{2+} are shown in **Supplementary Fig. 23a**. At a fully discharged state, the V_d-V_2O_3 electrode displays two Zn $2p_{3/2}$ components located at 1022.5 eV and 1023.2 eV which belong to the intercalated Zn^{2+} at different occupation sites (vanadium vacancies and tunnels nearby vanadium vacancies). At fully charged state, the Zn $2p_{3/2}$ peak located at 1023.2 eV disappears while the peak of 1022.5 eV is reserved. That is to say that some vanadium vacancies occupied Zn^{2+} is riveted in the lattice of V_d-V_2O_3, only enable Zn^{2+} reversibly (de)intercalation in the tunnel neighboring the remaining vanadium vacancies. Precise quantification of the V and Zn contents at fully dis/charged states was carried on the inductively coupled plasma emission spectroscopy (ICP-AES) and the detailed results show in **Supplementary Table 5**. The identical results can be gotten from TEM

elemental mapping where the Zn, V, and O elements are uniformly distributed (**Supplementary Figs. 24 and 25**). The charge compensation of V in the process of Zn^{2+} insertion/extraction is shown in the V L-edge patterns (**Figs. 4c and 4d**). Two peaks located at ~518 eV and 525 eV are observed in the V L-edge pattern, corresponding to V $2p_{3/2}$→V 3d and V $2p_{1/2}$→V 3d transitions, respectively[34,35]. The intensity of V $2p_{3/2}$ peaks are increased with the entrance of Zn^{2+} and decreased with the release of Zn^{2+}, gradually, stating the electronic acquirement and deprivation of V in the Zn^{2+} electrochemistry. Notably, under the same voltage, the peak intensity remains the same revealing the high reversibility of the V_d-V_2O_3 electrode. The valence changes in the whole cycle are also shown in the high-resolution XPS of V (**Supplementary Fig. 23b**) where the peak of V^{4+} becomes dominant upon charging while releasing a sign of a let-up upon discharging. Given the local environment of vacancy, the local chemical and electronic environment of intercalated Zn^{2+} was investigated by Zn K-edge XAFS. Since the surrounding local environment of Zn^{2+} is the same during charging and discharging, the K-edge XAFS of Zn is changeless (**Fig. 4e and Supplementary Fig. 26**).

Conclusion

In summary, we have quantified 5.7% V_d clusters in a V_d-V_2O_3 cathode for the first time in aqueous ZIBs which shows remarkable Zn^{2+} storage performance. The DFT calculations indicated that the Zn^{2+} storage reversibility and stability will be greatly enhanced under the effects of V_d clusters. Concretely, part of vanadium vacancies provides permanent sites for the preoccupation of a small amount of Zn^{2+} so that the

system will have a more stable structure to against collapsing during the process of Zn^{2+} insertion/extraction. Meanwhile, the other vanadium vacancies can effectively weaken the strong interaction between Zn^{2+} and V_2O_3 material host to allow free insertion/extraction of Zn^{2+}. Benefitting from the 5.7% V_d clusters, the V_d-V_2O_3 cathode provides a capacity of 196 mA h g^{-1} at 0.1 A g^{-1} and exhibits ultra-long stability up to 30,000 cycles with a capacity retention of 81%, which is the longest aqueous ZIBs stability as far as we know. This accurately quantifying and determining the effect of defects opens a new window for designing aqueous ZIBs cathodes with ultra-long stability.

Data availability

The data that support the plots within this paper and other findings of this study are available from the corresponding author upon reasonable request.

References

1. Larcher, D. & Tarascon, J. M. Towards greener and more sustainable batteries for electrical energy storage. *Nat. Chem.* **7**, 19-29 (2015).
2. Lu, Y., Goodenough, J. B. & Kim, Y. Aqueous cathode for next-generation alkali-ion batteries. *J. Am. Chem. Soc.* **133**, 5756-5759 (2011).
3. Idota, Y., Kubota, T., Matsufuji, A., Maekawa, Y. & Miyasaka, T. Tin-based amorphous oxide: a high-capacity lithium-ion-storage material. *Science* **276**, 1395-1397 (1997).
4. Bruce, P. G., Freunberger, S. A., Hardwick, L. J. & Tarascon, J. M. Li-O_2 and Li-S batteries with high energy storage. *Nat. Mater.* **11**, 19-29 (2011).
5. Goodenough, J. B. & Park, K. S. The li-ion rechargeable battery: a perspective. *J. Am. Chem. Soc.* **135**, 1167-1176 (2013).
6. Xia, C. *et al.* Rechargeable aqueous zinc-ion battery based on porous framework zinc pyrovanadate intercalation cathode. *Adv. Mater.* **30** (2018).
7. Pan, H. *et al.* Reversible aqueous zinc/manganese oxide energy storage from conversion reactions. *Nat. Energy.* **1** (2016).
8. Zhang, N. *et al.* Rechargeable aqueous zinc-manganese dioxide batteries with high energy and power densities. *Nat. Commun.* **8**, 405 (2017).

9. Yan, M. *et al.* Water-lubricated intercalation in $V_2O_5{\cdot}nH_2O$ for high-capacity and high-rate aqueous rechargeable zinc batteries. *Adv. Mater.* **30** (2018).
10. Li, H. *et al.* Waterproof and tailorable elastic rechargeable yarn zinc ion batteries by a cross-linked polyacrylamide electrolyte. *ACS Nano* **12**, 3140-3148 (2018).
11. Wan, F. *et al.* An aqueous rechargeable zinc-organic battery with hybrid mechanism. *Adv. Funct. Mater.* **28**, 1804975 (2018).
12. Li, H. *et al.* An extremely safe and wearable solid-state zinc ion battery based on a hierarchical structured polymer electrolyte. *Energy Environ. Sci.* **11**, 941-951 (2018).
13. Yoo, H. D. *et al.* Fast kinetics of magnesium monochloride cations in interlayer-expanded titanium disulfide for magnesium rechargeable batteries. *Nat. Commun.* **8**, 339 (2017).
14. Koketsu, T. *et al.* Reversible magnesium and aluminium ions insertion in cation-deficient anatase TiO_2. *Nat. Mater.* **16**, 1142-1148 (2017).
15. Sun, X., Bonnick, P. & Nazar, L. F. Layered TiS_2 positive electrode for Mg batteries. *ACS Energy Lett.* **1**, 297-301 (2016).
16. Liao, M. *et al.* A deep-cycle aqueous zinc-ion battery containing an oxygen-deficient vanadium oxide cathode. *Angew. Chem. Int. Ed.* **59**, 2273-2278 (2020).
17. Wang, Q., Zhang, Y., Zheng, J., Hu, T. & Meng, C. Synthesis, structure, optical and magnetic properties of interlamellar decoration of magadiite using vanadium oxide species. *Microporous and Mesoporous Mater.* **244**, 264-277 (2017).
18. Adamski, A., Spalek, T. & Sojka, Z. Application of EPR spectroscopy for elucidation of vanadium speciation in VOx/ZrO_2 catalysts subject to redox treatment. *Res. Chem. Intermed.* **29**, 793-804 (2003).
19. Yu, M. *et al.* Valence-optimized vanadium oxide supercapacitor electrodes exhibit ultrahigh capacitance and super-long cyclic durability of 100,000 cycles. *Adv. Funct. Mater.* **25**, 3534-3540 (2015).
20. Gou, W. *et al.* Yolk-shell structured V_2O_3 microspheres wrapped in N, S co-doped carbon as pea-pod nanofibers for high-capacity lithium ion batteries. *Chem. Eng. J.* **374**, 545-553 (2019).
21. Wong, J., Lytle, F. W., Messmer, R. P. & Maylotte, D. H. K-edge absorption spectra of selected vanadium compounds. *Phys. Rev. B* **30**, 5596-5610 (1984).
22. Zhao, Y. *et al.* Defect-rich ultrathin ZnAl-layered double hydroxide nanosheets for efficient photoreduction of CO_2 to CO with water. *Adv. Mater.* **27**, 7824-7831 (2015).
23. Liu, Y. *et al.* Heterogeneous spin states in ultrathin nanosheets induce subtle lattice distortion to trigger efficient hydrogen evolution. *J. Am. Chem. Soc.* **138**, 5087-5092 (2016).
24. Liu, X., Zhou, K., Wang, L., Wang, B., & Li, Y. Oxygen vacancy clusters promoting reducibility and activity of ceria nanorods. *J. Am. Chem. Soc.* **131**, 3140-3141 (2009).
25. Wan, F. *et al.* Aqueous rechargeable zinc/sodium vanadate batteries with enhanced performance from simultaneous insertion of dual carriers. *Nat. Commun.* **9**, 1656 (2018).
26. He, P. *et al.* Sodium ion stabilized vanadium oxide nanowire cathode for high-performance zinc-ion batteries. *Adv. Energy Mater.* **8**, 1702463 (2018).
27. Li, Z. *et al.* Mechanistic insight into the electrochemical performance of Zn/VO_2 batteries with an aqueous $ZnSO_4$ electrolyte. *Adv. Energy Mater.* **9**, 1900237 (2019).
28. Zhang, N. *et al.* Rechargeable aqueous $Zn–V_2O_5$ battery with high energy density and long cycle life. *ACS Energy Lett.* **3**, 1366-1372 (2018).
29. Kundu, D., Adams, B. D., Duffort, V., Vajargah, S. H. & Nazar, L. F. A high-capacity and long-life

aqueous rechargeable zinc battery using a metal oxide intercalation cathode. *Nat. Energy* (2016).
30. Liu, C. *et al.* Expanded hydrated vanadate for high-performance aqueous zinc-ion batteries. *Energy Environ. Sci.* **12**, 2273-2285 (2019).
31. Yang, Y. *et al.* Li^+ intercalated $V_2O_5 \cdot nH_2O$ with enlarged layer spacing and fast ion diffusion as an aqueous zinc-ion battery cathode. *Energy Environ. Sci.* **11**, 3157-3162 (2018).
32. Fang, G. *et al.* Suppressing manganese dissolution in potassium manganate with rich oxygen defects engaged high-energy-density and durable aqueous zinc-ion battery. *Adv. Funct. Mater.* **29**, 1808375 (2019).
33. Zhu, C. *et al.* Electrochemically induced cationic defect in MnO intercalation cathode for aqueous zinc-ion battery. *Energy Storage Mater.* **24**, 394-401 (2020).
34. Goering, E., Müller, O., Klemm, M., denBoer, M. L. & Horn, S. Angle dependent soft-X-ray absorption spectroscopy of V_2O_5. *Philos. Mag. B* **75**, 229-236 (2006).
35. Velazquez, J. M., Jaye, C., Fischer, D. A. & Banerjee, S. Near edge X-ray absorption fine structure spectroscopy studies of single-crystalline V_2O_5 nanowire arrays. *J. Phys. Chem. C* **113**, 7639–7645 (2009).

Acknowledgmwnts

This work was financially supported in part by the National Key R&D Program of China (2020YFA0405800), NSFC (U1932201, U2032113, 22075264), CAS Collaborative Innovation Program of Hefei Science Center (2019HSC-CIP002, 2020HSC-CIP002), CAS Interdisciplinary Innovation Team, and USTC Research Funds of the Double First-Class Initiative (Grant No. YD2310002003). L.S. acknowledges the support from Key Laboratory of Advanced Energy Materials Chemistry (Ministry of Education), Nankai University (111 project, B12015). The authors thank the Beijing Synchrotron Radiation Facility (1W1B, BSRF), Shanghai Synchrotron Radiation Facility (BL14W1, SSRF), the Hefei Synchrotron Radiation Facility (MCD-A and MCD-B Soochow Beamline for Energy Materials at NSRL), and the USTC Center for Micro and Nanoscale Research and Fabrication for helps in characterizations.

Author contributions

L.S. and S.M.C. supervised the project. K.F.Z. and S.Q.W. designed the work and carried out most of the experiments. L.H.H. and F.R.S. measured and analyzed XRD and NPD data. H.W.S. simulated most of the calculations. P.J.Z. and C.D.W. performed XAFS and sXAS experiments. Y.Y.C. and X.G. helped to prepare most of the samples. H.J.Z., B.J.Y., and M.L. guided the PAS measurements and helped to analyze PAS results. X.J.W. helped to explain some experimental data. All the authors discussed the results and assisted during the manuscript preparation.

Figure

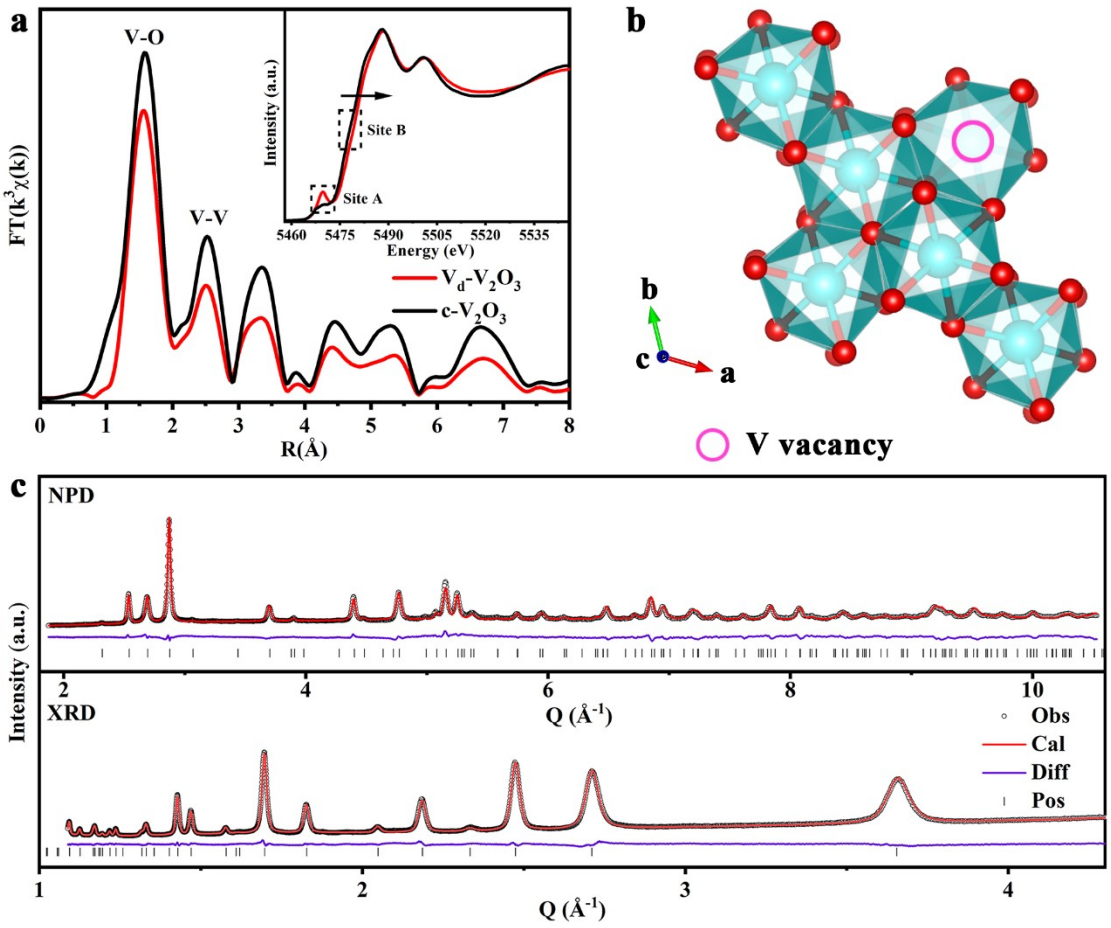

Fig. 1 | a, Normalized XANES spectrum of V_d-V_2O_3 and c-V_2O_3, inset: the corresponding Fourier-transformed V K-edge EXAFS spectra of V_d-V_2O_3 and c-V_2O_3. **b**, Schematic diagram of the structure of V_d-V_2O_3 along the c-axis. The oxygen atoms are represented by small red spheres, and the V atoms are depicted in blue. **c**, Observed (black circle), calculated diffraction patterns (red line), their difference (purple line) and peak position (black bar) of the NPD pattern (upper part) and XRD pattern (lower part).

Table 1 | Position lifetime parameters of V_d-V_2O_3 and c-V_2O_3.

Sample	τ_1 (ns)	τ_2 (ns)	τ_3 (ns)	I_1 (%)	I_2 (%)	I_3 (%)
V_d-V_2O_3	0.156	0.373	1.559	17.023	78.011	4.966
c-V_2O_3	0.175	0.392	1.610	57.085	37.943	4.972

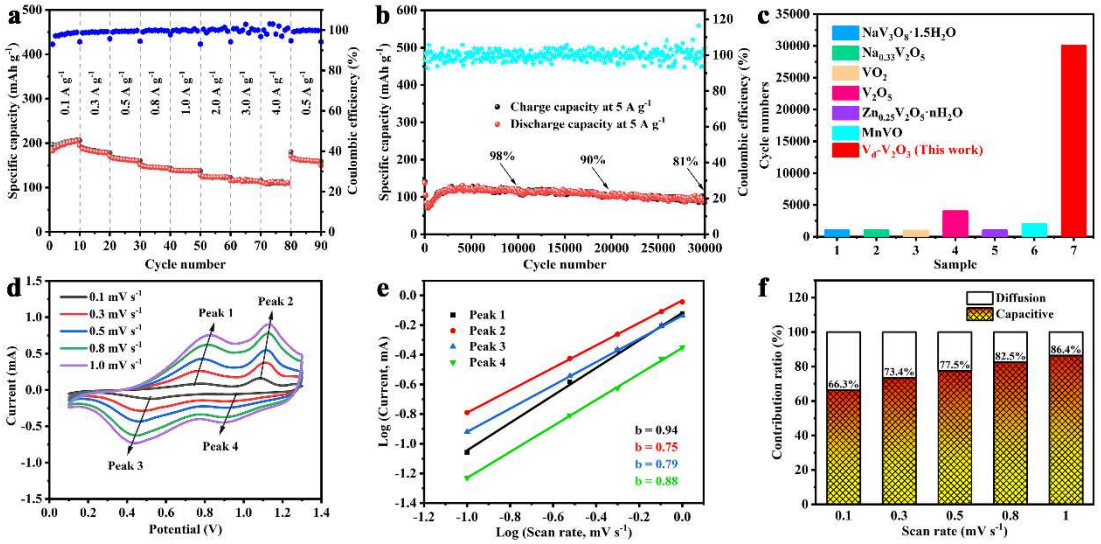

Fig. 2 | a, Rate performance at different current densities of V_d-V_2O_3 electrode. **b**, Long-term cycling performance and coulombic efficiency of V_d-V_2O_3 electrode at a current density of 5 A g^{-1}. **c**, Comparison of the cycle stability between V_d-V_2O_3 and other vanadium-based cathodes for aqueous zinc-ion batteries. **d**, CV curves of the V_d-V_2O_3 electrode at scan rates ranging from 0.1 to 1 mV s^{-1}. **e**, Log (*i*) versus log (*v*) plots at specific peak currents. **f**, Contribution ratios of capacitive and diffusion-controlled capacities at different scan rates from 0.1 mV s^{-1} to 1.0 mV s^{-1}.

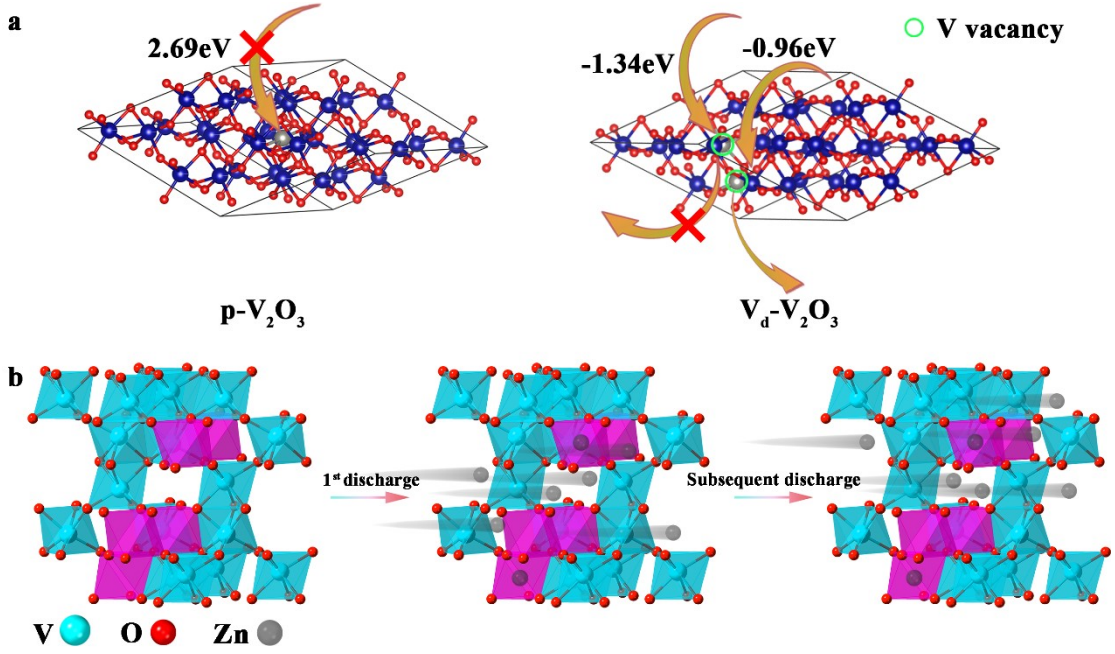

Fig. 3 | a, The Gibbs free energy of different models. **b**, The schematic illustration of the energy storage mechanism in the Zn/V_2O_3 battery.

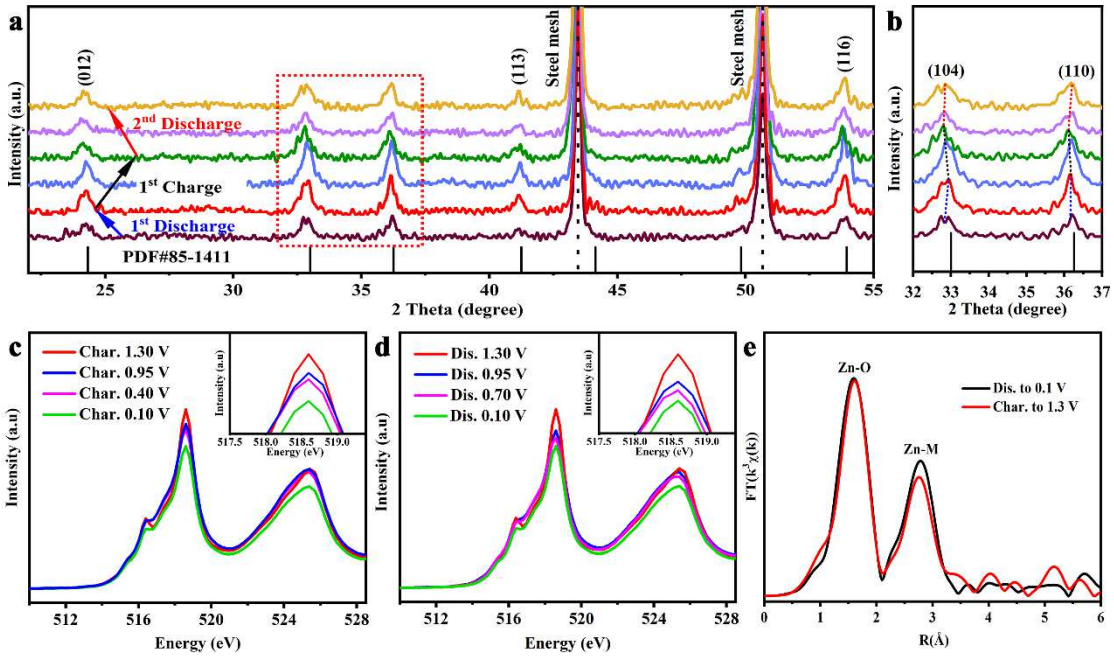

Fig. 4 | a, *Ex-situ* XRD patterns of V_d-V_2O_3 electrodes at different cut-off voltages during the charge and discharge process. **b**, An enlarged view of the red dotted frame in Figure 4a. **c**, Normalized XANES spectrum of the V L-edge for V_d-V_2O_3 electrodes at different voltages during the charging process. **d**, Normalized XANES spectrum of the V-edge for V_d-V_2O_3 electrodes at different voltages during the discharging process. **e**, Fourier-transformed Zn K-edge EXAFS spectra of V_d-V_2O_3 electrodes at fully charged and discharged states.

TOC

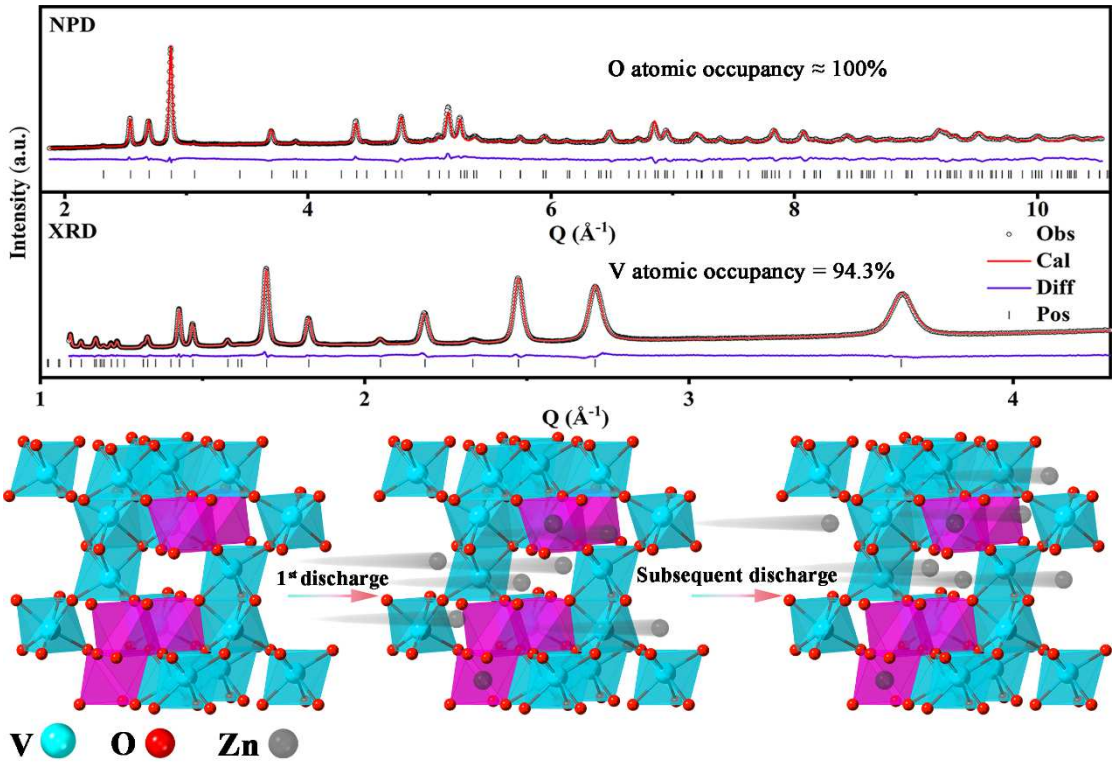
NPD
O atomic occupancy ≈ 100%
Intensity (a.u.)
2
4
6
8
10
XRD
Q (Å-1)
Obs
Cal
Diff
Pos
V atomic occupancy = 94.3%
1
2
3
4
Q (Å-1)
1st discharge
Subsequent discharge
V
O
Zn

Figures

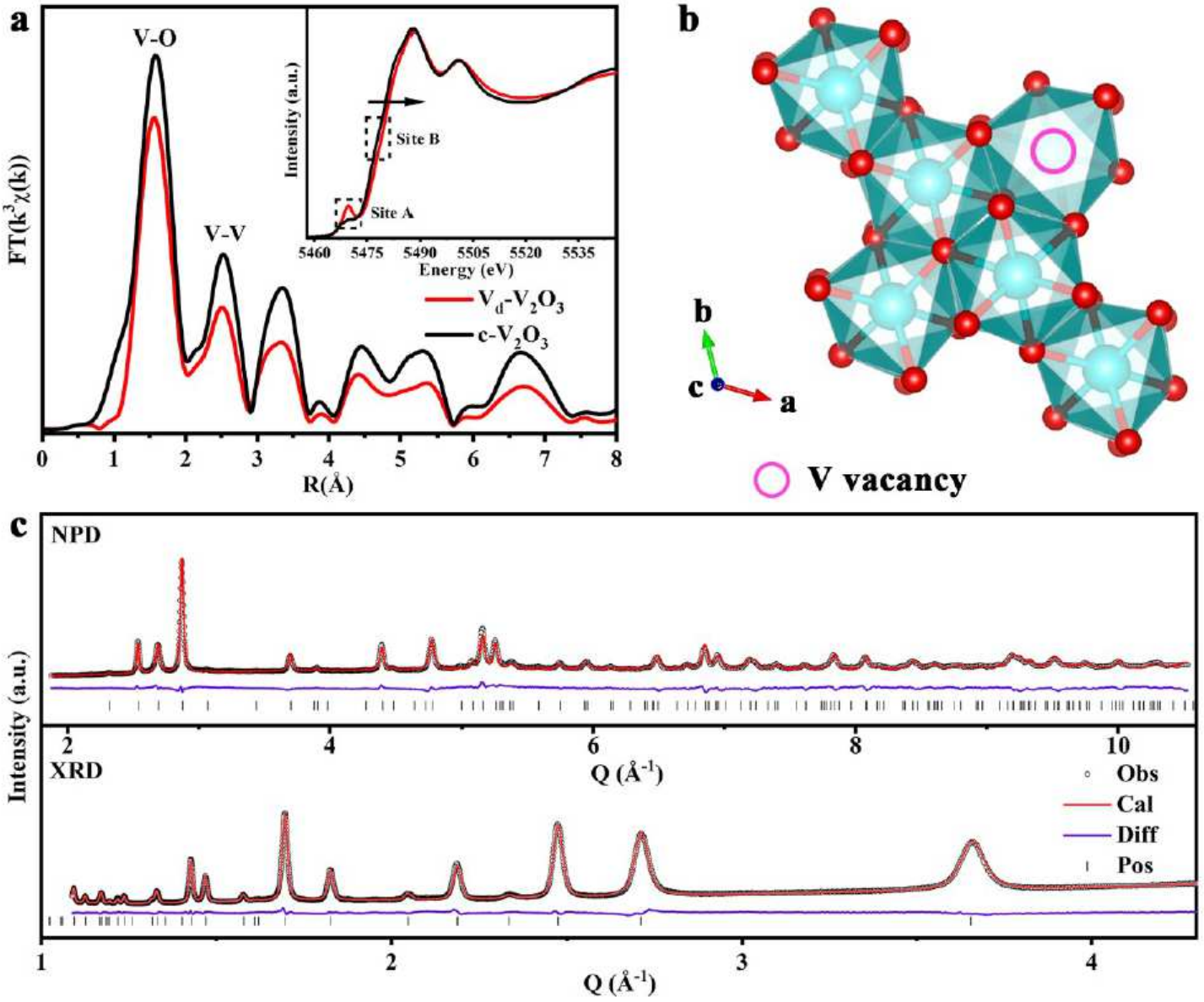

Figure 1

a, Normalized XANES spectrum of Vd-V2O3 and c-V2O3, inset: the corresponding Fourier-transformed V K-edge EXAFS spectra of Vd-V2O3 and c-V2O3. b, Schematic diagram of the structure of Vd-V2O3 along the c-axis. The oxygen atoms are represented by small red spheres, and the V atoms are depicted in blue. c, Observed (black circle), calculated diffraction patterns (red line), their difference (purple line) and peak position (black bar) of the NPD pattern (upper part) and XRD pattern (lower part). Table 1 | Position lifetime parameters of Vd-V2O3 and c-V2O3.

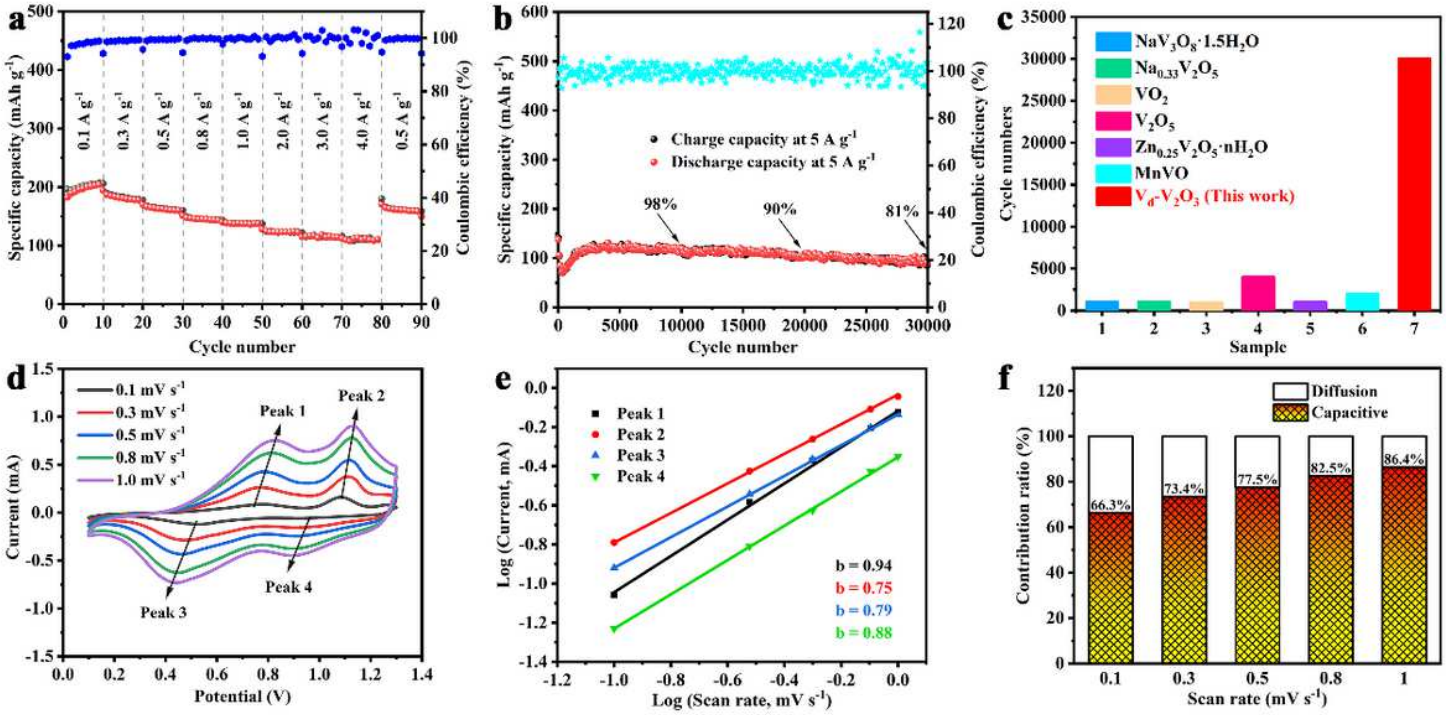

Figure 2

a, Rate performance at different current densities of Vd-V2O3 electrode. b, Long-term cycling performance and coulombic efficiency of Vd-V2O3 electrode at a current density of 5 A g-1. c, Comparison of the cycle stability between Vd-V2O3 and other vanadium-based cathodes for aqueous zinc-ion batteries. d, CV curves of the Vd-V2O3 electrode at scan rates ranging from 0.1 to 1 mV s-1. e, Log (i) versus log (v) plots at specific peak currents. f, Contribution ratios of capacitive and diffusion-controlled capacities at different scan rates from 0.1 mV s-1 to 1.0 mV s-1.

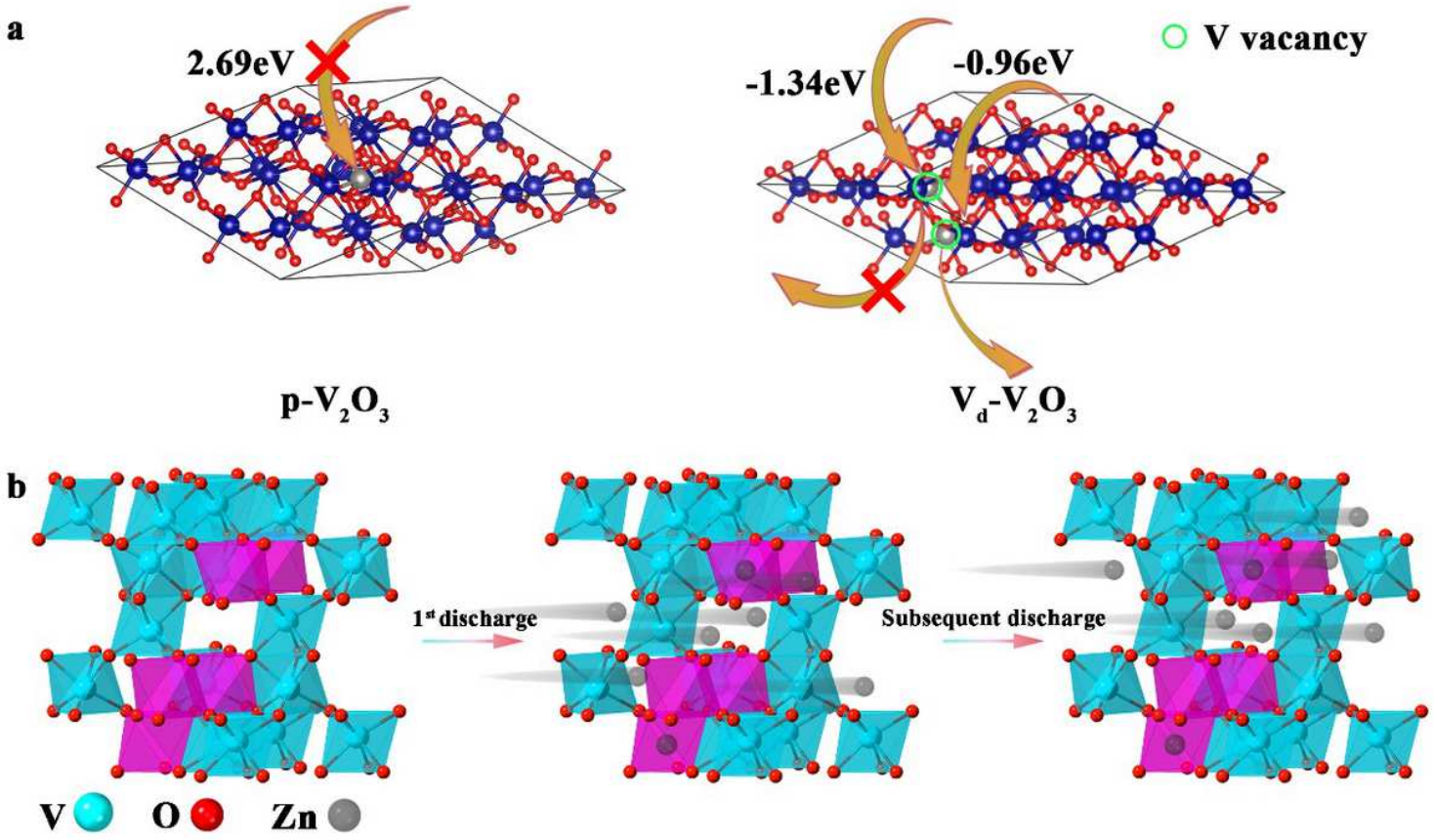

Figure 3

a, The Gibbs free energy of different models. b, The schematic illustration of the energy storage mechanism in the Zn/V2O3 battery.

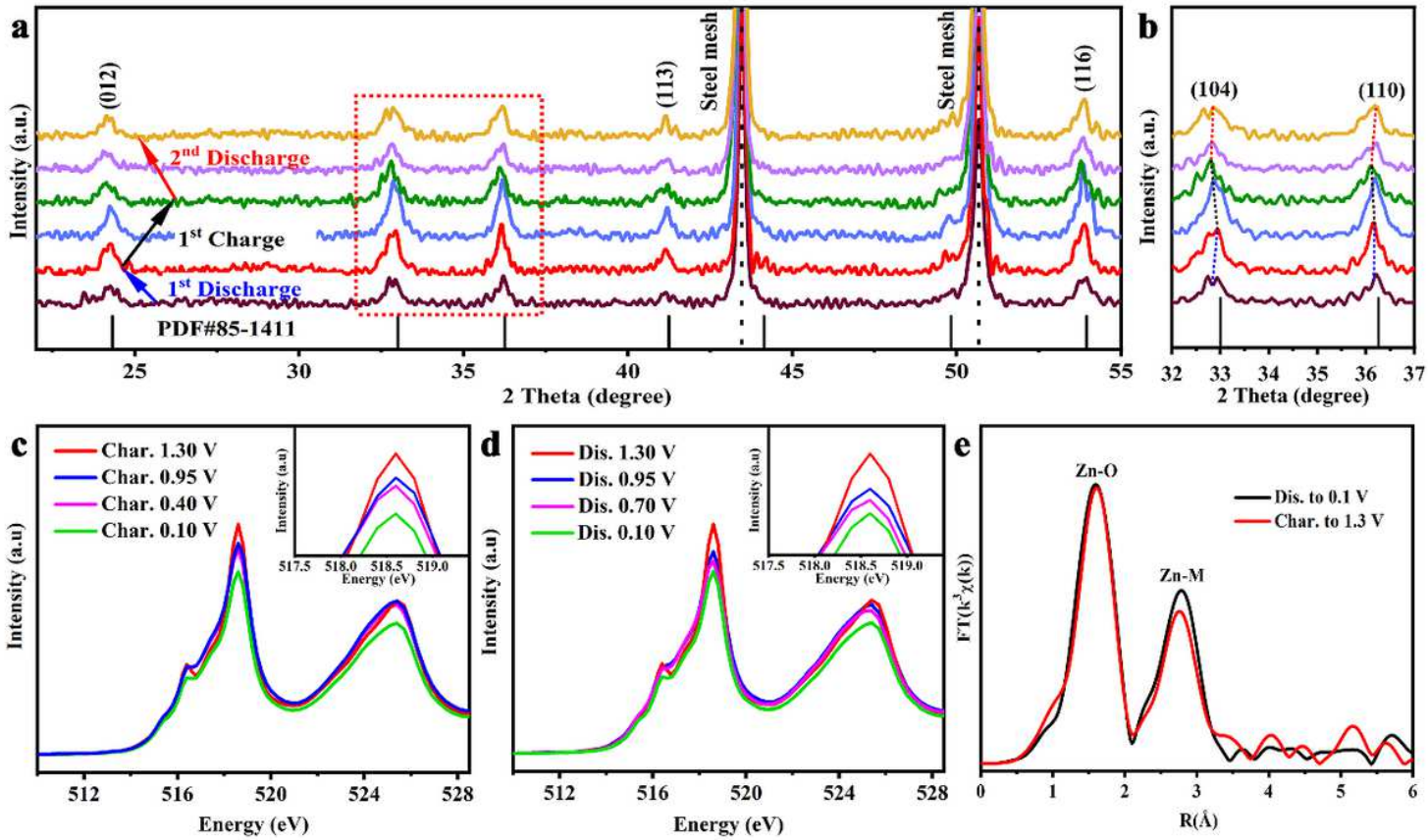

Figure 4

a, Ex-situ XRD patterns of Vd-V2O3 electrodes at different cut-off voltages during the charge and discharge process. b, An enlarged view of the red dotted frame in Figure 4a. c, Normalized XANES spectrum of the V L-edge for Vd-V2O3 electrodes at different voltages during the charging process. d, Normalized XANES spectrum of the V-edge for Vd-V2O3 electrodes at different voltages during the discharging process. e, Fourier-transformed Zn K-edge EXAFS spectra of Vd-V2O3 electrodes at fully charged and discharged states.

Supplementary Files

This is a list of supplementary files associated with this preprint. Click to download.

- SupplementaryInformation.pdf